Water Resources Research

RESEARCH ARTICLE
10.1029/2018WR023214

Key Points:
- The local capillary pressure was measured and quantified during imbibition using a pore-scale curvature-based image analysis
- The relative permeability was found from the measured pressure drop with an analytical correction for the capillary pressure gradient
- The capillary pressure and relative permeability can be measured directly and simultaneously in the flow experiment

Correspondence to:
Q. Lin,
q.lin11@imperial.ac.uk

Citation:
Lin, Q., Bijeljic, B., Pini, R., Blunt, M. J., & Krevor, S. (2018). Imaging and measurement of pore-scale interfacial curvature to determine capillary pressure simultaneously with relative permeability. *Water Resources Research*, *54*. https://doi.org/10.1029/2018WR023214

Received 27 APR 2018
Accepted 5 SEP 2018
Accepted article online 10 SEP 2018

Imaging and Measurement of Pore-Scale Interfacial Curvature to Determine Capillary Pressure Simultaneously With Relative Permeability

Qingyang Lin[1], Branko Bijeljic[1], Ronny Pini[2], Martin J. Blunt[1], and Samuel Krevor[1]

[1]Department of Earth Science and Engineering, Imperial College London, London, UK, [2]Department of Chemical Engineering, Imperial College London, London, UK

Abstract There are a number of challenges associated with the determination of relative permeability and capillary pressure. It is difficult to measure both parameters simultaneously on the same sample using conventional methods. Instead, separate measurements are made on different samples, usually with different flooding protocols. Hence, it is not certain that the pore structure and displacement processes used to determine relative permeability are the same as those when capillary pressure was measured. Moreover, at present, we do not use pore-scale information from high-resolution imaging to inform multiphase flow properties directly. We introduce a method using pore-scale imaging to determine capillary pressure from local interfacial curvature. This, in combination with pressure drop measurements, allows both relative permeabilities and capillary pressure to be determined during steady state coinjection of two phases through the core. A steady state waterflood experiment was performed in a Bentheimer sandstone, where decalin and brine were simultaneously injected through the core at increasing brine fractional flows from 0 to 1. The local saturation and the curvature of the oil-brine interface were determined. Using the Young-Laplace law, the curvature was related to a local capillary pressure. There was a detectable gradient in both saturation and capillary pressure along the flow direction. The relative permeability was determined from the experimentally measured pressure drop and average saturation obtained by imaging. An analytical correction to the brine relative permeability could be made using the capillary pressure gradient. The results for both relative permeability and capillary pressure are consistent with previous literature measurements on larger samples.

1. Introduction

The understanding and characterization of multiphase fluid flows within geological porous media are important in many applications including hydrocarbon recovery, carbon storage, and contaminant transport (Blunt et al., 2013; Fredd & Fogler, 1998; Gaus et al., 2008; Gelhar et al., 1992; Morrow & Buckley, 2011; Parker, 1989). Fluids move through the complex capillary system comprising the pore space of the rock. At scales larger than a millimeter, the practicalities of rock characterization and computational demands preclude the modeling of fluid flow directly through this geometry, and a continuum approach is taken to model subsurface flows. Multiphase flow is controlled by two critical parameters, which account for the impact of interfacial forces on the fluid distribution and movement. These are the capillary pressure and the relative permeability of each phase, both assumed to be functions of the wetting phase (brine) saturation, (S_w) (Blunt, 2017; Herring et al., 2017; Muskat & Meres, 1936; Parker, 1989; Richards, 1931). There are, however, longstanding limitations in the use of this formulation to accurately predict subsurface fluid flow at the scales of tens of meters to kilometers, some of which are linked to the upscaled representation of the small—pore to meter—scale fluid dynamics.

We summarize the continuum approach using the brine-oil system as an example, where brine is the wetting phase, and oil is the nonwetting phase. The relative permeability for each phase can be described through the multiphase Darcy law for one-dimensional horizontal flow (Blunt, 2017; Whitaker, 1986):

$$q_w = -\frac{kk_{rw}}{\mu_w}\frac{dP_w}{dx} \tag{1}$$

$$q_o = -\frac{kk_{ro}}{\mu_o}\frac{dP_o}{dx} \tag{2}$$

where q is the Darcy flow rate, k_r is the relative permeability, μ is the viscosity, and P is the pressure. The subscripts o and w refer to the oil and water (brine) phases, respectively. The k is the absolute permeability. The x represents the flow direction along the sample length. The capillary pressure P_c is defined as the pressure difference between the oil and brine:

$$P_c = P_o - P_w \tag{3}$$

Traditionally, capillary pressure is measured independently on different samples from those used in the relative permeability tests (Loeve et al., 2011; Masalmeh et al., 2004; Masalmeh & Jing, 2008). The porous plate method, the mercury intrusion capillary pressure method (MICP), and the centrifuge method are the three most widely used techniques (Darling, 2005; Hassler & Brunner, 1945; Kalam et al., 2006; Pini et al., 2012). These tests are routinely used in the oil industry as a part of reservoir characterization known as Special Core Analysis (SCAL; Darling, 2005; Masalmeh & Jing, 2008).

The porous plate method is considered to be the most accurate and reliable method as it ensures a homogeneous saturation profile, allows the use of reservoir fluids, and can be used for both drainage and waterflood processes (Kalam et al., 2006). The main limitation of this method is that it is time-consuming, taking up to a few months to obtain the capillary pressure over the full range of saturation (Kennedy, 2015). MICP measurements are much faster, but this technique is destructive, only studies a small sample volume (~cm^3), uses mercury as the injection fluid whose wettability may be very different from a reservoir crude oil/brine system, and can only study drainage reliably. Centrifugation is another method to obtain capillary pressure, but here the signal is strongly influenced by sample boundary-effects, and it is difficult to apply reservoir conditions (Kalam et al., 2006). Finally, in none of these methods is the relative permeability also directly measured at the same time. At the core scale, a multirate drainage experiment can be performed by injecting nonwetting phase to obtain the drainage capillary pressure and relative permeability simultaneously at steady state (Pini et al., 2012; Pini & Benson, 2013). However, this method cannot provide the relative permeability for the wetting phase. There would be a significant increase in the robustness of these observations if relative permeability and capillary pressure could be observed simultaneously, eliminating concerns over the reproducibility of samples and displacement sequences.

For relative permeability, the steady state method is widely considered to provide the most reliable results in the midsaturation range (McPhee et al., 2015). Here a stable fluid distribution at a known fractional flow, f_w, is established while the saturation and pressure drop are recorded. If we assume that the pressure in the oil phase is measured, then from equation (1)–(3) we may write

$$f_w = \frac{q_w}{q_w + q_o} = \frac{\lambda_w\left(1 - \frac{dP_c}{dx} / \frac{dP_o}{dx}\right)}{\lambda_o + \lambda_w\left(1 - \frac{dP_c}{dx} / \frac{dP_o}{dx}\right)} \tag{4}$$

where λ is the mobility defined as kk_r/μ. We can then define

$$R = \frac{dP_c}{dx} / \frac{dP_o}{dx} = \frac{dP_c}{dP_o} \tag{5}$$

$$f_w = \frac{\lambda_w(1 - R)}{\lambda_t - R\lambda_w} \tag{6}$$

where $\lambda_t = \lambda_o + \lambda_w$. Since q_t and f_w are known, the relative permeabilities can be obtained as

$$k_{ro} = \frac{\mu_o L(1 - f_w)q_t}{k\Delta P_o} \tag{7}$$

$$k_{rw} = \frac{\mu_w L f_w q_t}{k\Delta P_o(1 - R)} \tag{8}$$

where ΔP_o is the measured pressure drop in the oil phase over a length L. If we assume that the saturation and the capillary pressure are both constant, and hence $R = 0$, we can find the relative permeabilities. This is the approach used in traditional steady state relative permeability core-flood experiments.

At the centimeter scale, gradients in capillary pressure are the dominant controls on the fluid saturation distribution, while the viscous effects, encapsulated in the terms without capillary pressure in the multiphase Darcy law, are relatively small (Zhou et al., 1997). In laboratory tests, capillary pressure discontinuities at the inlet and outlet boundaries of the rock core are the source of the capillary end effect. As a consequence, any variation in capillary pressure is likely to lead to significant perturbations of the flow and render the brine relative permeability estimated using equation (8) with $R = 0$ inaccurate, since R is not necessarily negligible. As a result commercial petrophysics laboratories also make use of numerical history matching software to remove the impacts of capillary pressure gradients (Archer & Wong, 1973), but this requires an estimate of capillary pressure, which as we have already discussed, is not determined directly on the same sample.

In the reservoir, there is significant natural capillary heterogeneity throughout the rocks. The impact of this heterogeneity can be represented using upscaled flow functions if the heterogeneity can be accurately characterized in the laboratory (Li & Benson, 2015; Rabinovich et al., 2015). However, this characterization, like the capillary end effect, requires a numerical history match of core-flood observations (Jackson et al., 2018; Krause, 2012; Sigmund & McCaffery, 1979) and incurs similar uncertainty around the uniqueness of the inferred multiphase flow properties.

Direct observations of pore-scale fluid curvature with simultaneous macroscopic measurements of relative permeability would eliminate the need for the numerical history matching approach to characterizing multiphase flow properties. Obtaining these two quantities directly avoids the use of simplifying assumptions and the uncertainties around uniqueness characteristic of the history matching approach. Furthermore, the measurement of interfacial curvature allows the determination of a local capillary pressure within the rock. The key aim of this work is to obtain a valid continuum property—the capillary pressure-saturation relationship—from the fluid interface curvature at the pore scale.

In recent years, pore-scale X-ray microtomography (micro-CT) imaging has been widely used in geologically related studies (Al-Khulaifi et al., 2018; Al-Menhali et al., 2016; Andrew et al., 2014a; Berg et al., 2013; Blunt et al., 2013; Cnudde & Boone, 2013; Ketcham & Carlson, 2001; Lai et al., 2015; Lin et al., 2018; Lin, Al-Khulaifi, et al., 2016; Lin, Neethling, et al., 2016; Qajar & Arns, 2016; Reyes et al., 2017; Reynolds et al., 2017; Saif et al., 2017; Schlüter et al., 2016). In particular, imaging of multiphase flow in porous rock has been performed, covering a wide range of topics, including wettability characterization based on contact angle measurement, relative permeability, and curvature analysis in the pore space to estimate capillary pressure (Akbarabadi & Piri, 2013; Alhammadi et al., 2017; AlRatrout et al., 2017; Andrew et al., 2014b; Armstrong, Pentland, et al., 2012; Arns et al., 2003; Berg et al., 2016; Gao et al., 2017; Garing et al., 2017; Herring et al., 2017; Krevor et al., 2012; Lin et al., 2017; Lv et al., 2017; Norouzi Apourvari & Arns, 2016).

Most relevant to this work are methods to estimate the interfacial curvature using a triangulated surface generated from segmented images (Armstrong, Pentland, et al., 2012; Li et al., 2018). The estimated curvature is sensitive to the voxel size, image quality, the amount of smoothing, and the segmentation method, which is evident from the range of values obtained across a single surface (Armstrong, Pentland, et al., 2012; Garing et al., 2017; Li et al., 2018). However, at a fixed voxel size, the average curvature remains constant after a certain amount of smoothing (Andrew et al., 2014b; Garing et al., 2017; Li et al., 2018), which is used in this study to indicate the average capillary pressure.

We build on these works to simultaneously measure the pore-scale characteristics of fluid distribution and fluid curvature in steady state two-phase flow experiments where the average pressure differential is simultaneously measured. The observations are made during imbibition in an oil-brine system, in a quartz-rich sandstone rock core. The suite of observations allows us to directly evaluate capillary pressure and relative permeability simultaneously and independently of each other. By combining traditional continuum-scale observational techniques with those of newly developed pore scale observations, our approach tackles key limitations in traditional core analysis, while extending the utility of measurements obtained at the pore scale.

2. Materials and Methods

2.1. Rock Samples and Fluid Properties

The rock used in this study is Bentheimer sandstone, containing 98% quartz, 1% kaolinite/chlorite, and 1% microcline (from X-ray diffraction analysis conducted by Panterra Geoconsultants, Netherlands). The

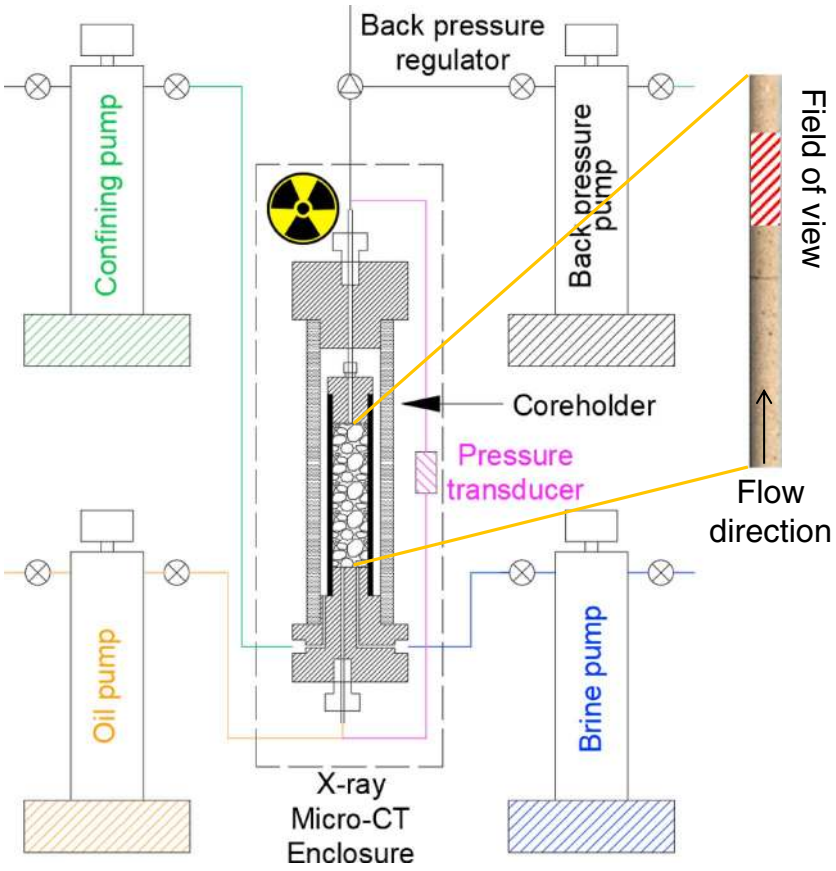

Figure 1. Schematic diagram of the experimental apparatus, showing the pump system for flow control and the design of the dual injection head for oil and brine (the brine pump and oil pump can inject fluid into the sample simultaneously). Tomographic scans were taken for the middle section of the downstream core over a vertical distance of 10.4 mm.

average porosity of the sample is 0.24 (measured by Autopore 9520, Micromeritics). The micro-CT samples were drilled into cylindrical cores 6.1 mm in diameter and 25.8 mm in length. The absolute permeability, measured at the same experimental conditions, is $1.47 \times 10^{-12} \pm 0.03 \times 10^{-12}$ m^2 (k = 1.49 ± 0.03 D). This was measured by injecting a single phase brine (3.5 wt % KI) while recording the pressure drop using the apparatus shown in Figure 1.

The brine solution was made from deionized water with a prescribed amount of potassium iodide (KI). KI was used as a solution contrast agent to enhance X-ray imaging. It has a high atomic weight and a correspondingly high X-ray attenuation coefficient. In this study the 3.5 wt % KI solution resulted in brine showing an intermediate grayscale value between the rock and oil in the X-ray imagery. Decalin (cis and trans decahydronaphthalene mixture with a dynamic viscosity of 3 mPa·s at 20 °C, supplied by Alfa Aesar) was selected as the nonwetting oil phase. The viscosity of the oil, μ_o, is approximately 3 times higher than the brine, μ_w ($\mu_o/\mu_w = 3$). The interfacial tension between brine and decalin was measured to be 51.5 mN/m, at ambient conditions measured by a Rame-Hart apparatus (590 F4 series) using the pendant drop method (Andreas et al., 1937; Stauffer, 1965).

2.2. Experimental Methodology

The steady state flow experiment was conducted using the apparatus shown in Figure 1, which is described in more detail in Gao et al. (2017). The experiments were conducted in a Hassler type flow cell made of carbon fiber epoxy with low X-ray photon attenuation. An injection head was designed, which allows oil and brine to be injected into the sample through separate inlet points simultaneously. This avoids discrete slugs of each fluid phase entering the rock, which can occur if both fluids are forced through a single capillary. Due to the

high permeability of the Bentheimer sample, two microcores were assembled in series (51.6 mm in total length) to enhance the pressure signal.

In this study, steady state conditions were reached in sequence through injecting at different fraction flows (f_w = 0, 0.05, 0.15, 0.3, 0.5, 0.85, 1) with a total flow rate of 0.02 ml/min. The total injection occurred over a period of at least 12 hr for each fractional flow step. The waiting time for each fractional flow varied: we waited until the differential pressure was constant over a period of at least 1-hr. The maximum capillary number ($Ca = \mu V/\sigma$, where V is the average velocity of the invading fluid, μ is the viscosity of the invading fluid, and σ is the brine-oil interfacial tension) for the oil phase was 6.6×10^{-7} when the fraction flow f_w = 0.

The experiment was conducted using the following procedure:

1. A confining pressure of 2 MPa was applied and maintained within the cell to compress the Viton sleeve around the core sample to avoid fluid bypass.
2. Scans of the air saturated rock sample were taken at room temperature.
3. The core was flooded with gaseous CO_2 for 30 min to remove air.
4. The core was flooded with brine (doped with 30 wt% KI). After 100% brine saturation was achieved, scans were taken of the brine saturated rock sample to characterize the porosity distribution including porosity below image resolution using differential imaging. The detailed procedure can be found in (Lin, Al-Khulaifi, et al., 2016). This allows the brine saturation to be accurately calculated.
5. The core was then flooded with brine (doped with 3.5 wt% KI) again for 1,000 pore volumes to replace the high salinity brine in the previous step.
6. Oil was injected at a flow rate of 5 ml/min to initialize the imbibition steps with a low initial brine (3.5 wt% KI) saturation.
7. The flow rate of oil was then reduced to 0.02 ml/min (f_w = 0). After reaching steady state, which can be indicated by the differential pressure transducer measurements, scans were taken to obtain the initial brine saturation.
8. Brine and oil were both injected at the same time at f_w = 0.05, with a total flow rate of 0.02 ml/min. Injection continued until steady state was achieved indicated by a stable pressure differential. Then a scan was taken.
9. Step 8 was repeated with different fractional flows f_w = 0.15, 0.3, 0.5, 0.85, 1 while keeping the total volumetric flow rate constant at 0.02 ml/min. Scans were taken once steady state had been reached for each fractional flow.
10. Steps 5–9 were also repeated without a sample inside the core holder to record the pressure dissipation due to the flow resistance of the core holder alone.
11. The differential transducer used in this study was a Keller PD-33X, with an accuracy of ±0.3 kPa. A back pressure of 500 kPa was applied through the entire experiment.

All the scans were taken using a Zeiss Versa 510 X-ray microscope with a flat panel detector, while fluids were flowing at steady state. The voxel size of the images was 3.58 μm. At each steady state point with different fractional flows, three scans were captured and stitched to a larger field of view (10.4 mm in length). The scanning parameters for each scan were 80 keV, 7 W, 0.04 s exposure time, and 3,201 projections. The full size of the scanned cylindrical sample is 1,700 × 1,700 × 4,000 (with cone effect), a subvolume 1,000 × 1,000 × 3,000 voxels has been analyzed in this study.

2.3. Image Preprocessing, Segmentation, and Fluid Curvature

After reconstruction and vertical stitching, all the images were registered to the dry scan image to have the same orientation using normalized mutual information and resampled using the Lanczos algorithm (Burger & Burge, 2010). Before extracting information from image analysis, a nonlocal means edge preserving filter (Buades et al., 2008) was applied to all the images to reduce the image noise.

The filtered grayscale image was segmented into three phases (rock grains, brine, and oil) by the use of a seeded watershed algorithm, where a seed was generated using a two-dimensional histogram of both the gray scale and the grayscale gradient images (Andrew et al., 2014b; Jones et al., 2007).

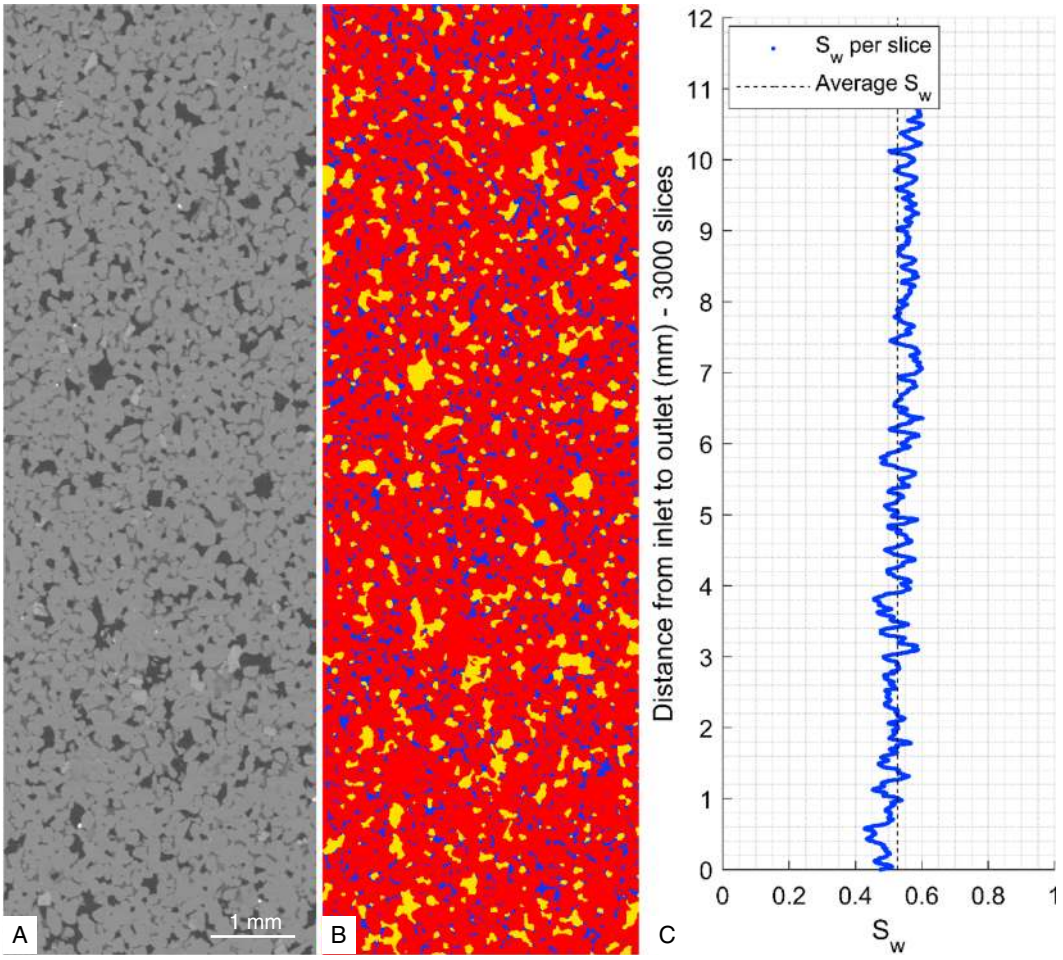

Figure 2. (a) Grayscale two-dimensional cross section of the three-dimensional image of the sample after applying a non-local means edge preserving filter. (b) Three-phase segmentation showing rock grains (red), brine (blue), and oil (yellow). (c) The saturation averaged in each slice along the direction of flow. The average saturation for the entire volume is 0.53. The thickness for each slice is 3.58 μm.

In pore-scale imaging where the interface between the wetting (brine) phase and nonwetting (oil) phase can be captured, the capillary pressure can be calculated from the curvature using the Young-Laplace law:

$$P_c = 2\sigma\kappa \tag{9}$$

where σ is the interfacial tension between the brine and oil phases and κ is the mean curvature of the interface, which can be defined as the average of the two principal curvatures. The curvature is found by approximating the surface locally as a quadratic form. The eigenvalues and eigenvectors of this quadratic form represent the principal curvature values and the directions of principal curvature, respectively. A surface scalar field is produced where the principal radii of curvature are averaged and assigned to each element across the interface (Andrew et al., 2014b; Armstrong, Porter, & Wildenschild, 2012). The curvature in this study was obtained using Avizo 9.3.0.

Here a curvature analysis for the interface between wetting and nonwetting phases was performed for a steady state experiment. A field of view 10.4 mm in vertical length was imaged with a voxel size of 3.58 μm. After image segmentation, the interface between oil and brine was captured and visualized. The interface was then extracted for surface processing and curvature analysis. After identifying the oil/brine interface, a smoothed surface was generated across the interface using a generalized marching cubes algorithm (Andrew et al., 2014b; Hege et al., 1997; Lorensen & Cline, 1987). The magnitude of

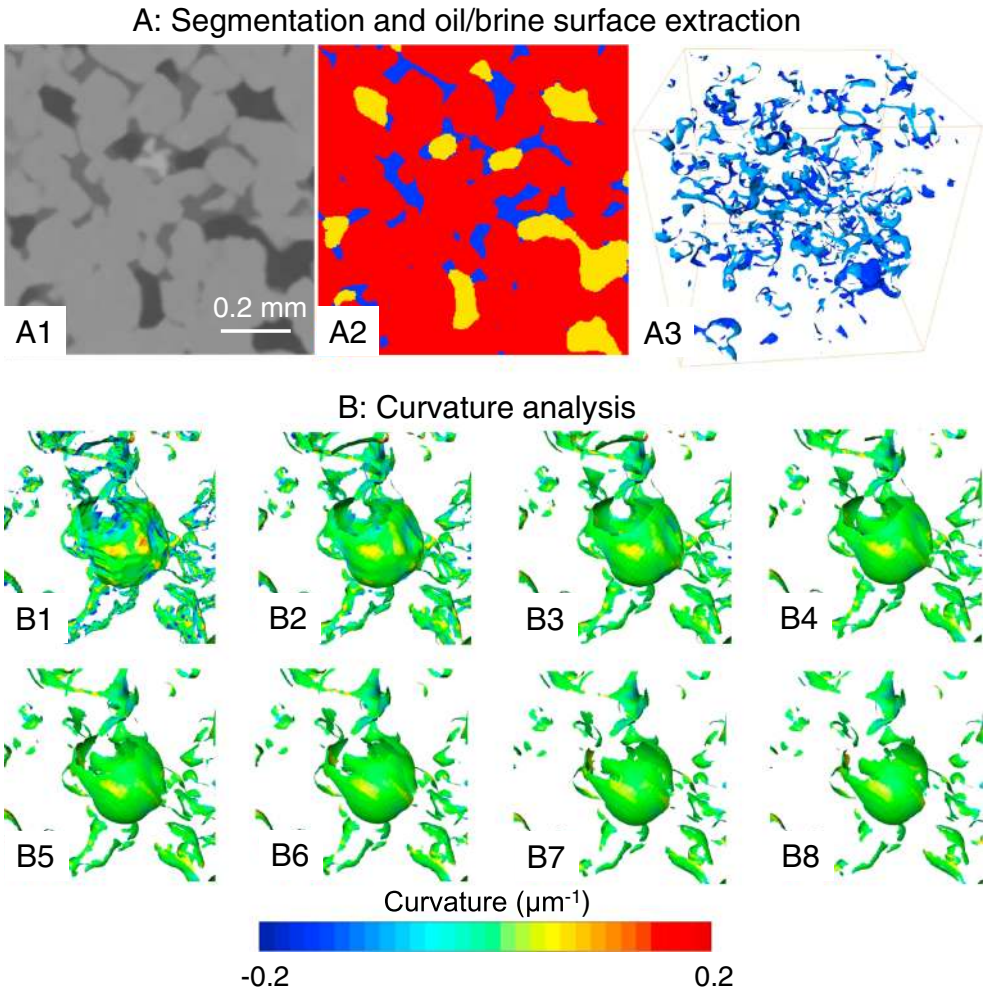

Figure 3. Surface identification, smoothing, and curvature calculation using a 250 × 250 × 250 voxel data set. (a) Oil/brine interface extraction based on three-phase segmentation (A1 to A3). A1 is the grayscale image showing oil (the darkest voxels), brine (intermediate gray voxels), and rock grains (the brightest voxels). A2 is the three-phase segmented image showing rock grains (red), brine (blue), and oil (yellow). A3 is the extracted oil/brine interface. (b) Computed curvature map. The surface is smoothed with different kernel sizes from 1 to 8 voxels (B1 to B8).

smoothing across the interface was altered by changing the size of the kernel of a modified Gauss filter used to compute probability weights during the surface assignment. The impact of the smoothing on the inferred distribution in curvature was used to decide on an optimal kernel, for example, the minimum level of smoothing beyond which the character (mean and variance) of the observed curvature distribution remained constant.

3. Results and Discussion

In the following, images obtained at f_w = 0.5 are used to demonstrate the method of image segmentation (section 3.1), the determination of capillary pressure and its variation from curvature measurements (section 3.2 and section 3.3), and the correction of relative permeability measurements for gradients in capillary pressure (section 3.4). Then the results from all fractional flows are used to construct relative permeability and capillary pressure, as well as to assess oil phase connectivity.

3.1. Image Segmentation and 1-D Saturation Profile

The results of the image segmentation are shown in Figure 2. The average brine saturation for the scanned region is 0.53 (computed from the entire volume). A saturation gradient can be observed in Figure 2c, indicative of a capillary pressure gradient from the inlet to the outlet of the sample. This provides an

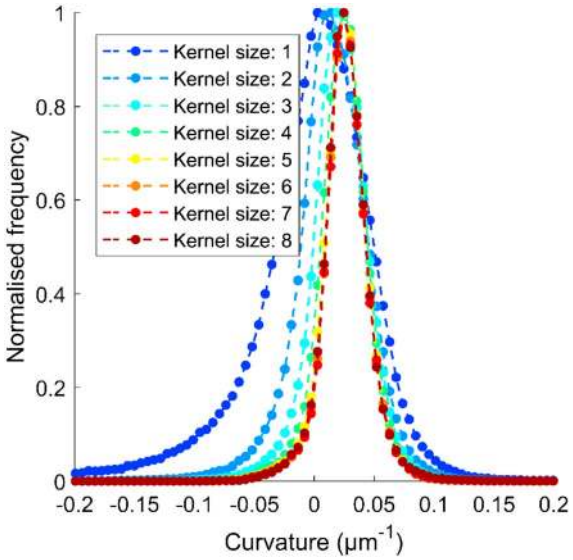

Figure 4. Frequency distributions of the curvature of the oil-brine interface with different smoothing kernel sizes. A kernel size of 5 voxels was used to infer the capillary pressure.

independent observation with which to benchmark the direct inference of capillary pressure from the analysis of fluid curvature.

3.2. Curvature Analysis

The results of the interface extraction and the impacts of smoothing on curvature are shown in Figure 3. The corresponding surfaces are shown in Figure 3b. The larger the kernel size (Armstrong, Pentland, et al., 2012), the smoother the surface and more uniform curvature distribution, and the narrower the distribution of the mean curvature (Figures 3b and 4).

In the curvature distribution (Figure 4), and capillary pressure distribution (Figure 5), there is measurement uncertainty caused primarily by image segmentation. The uncertainties can be estimated by the width of the distribution and the number of voxels with negative values at steady state. Because this is a water-wet system, all of the curvature values should be positive.

The error appears random, and surface smoothing preferentially eliminates the negative values while preserving the average value of curvature and capillary pressure. The impact of the smoothing kernel size on the frequency histogram of the curvature distribution is shown in Figure 4, where the width of the distribution and the number of negative values are significantly reduced when the smoothing kernel size increases. As the kernel size increases from 1 to 8 voxels, the percentage of points with negative curvature values decreases from 45 to 7.5%. When the kernel size is 5 voxels or greater, the curvature distributions no longer change significantly. The average curvature for the distribution, which is used as the macroscopic capillary pressure for the system, changes by less than 1%. We therefore use the average curvature with kernel size of 5 to estimate the capillary pressure.

These observations of uncertainty are consistent with other studies, which have quantified the likely error in the measurements (Andrew et al., 2014b; Armstrong, Pentland, et al., 2012; Garing et al., 2017). In particular, Li et al. (2018) performed an error analysis by using capillary tubes with different known radii. The curvature measurement error was up to approximately 9% with a minimum radius of 10 pixels. In this study, the

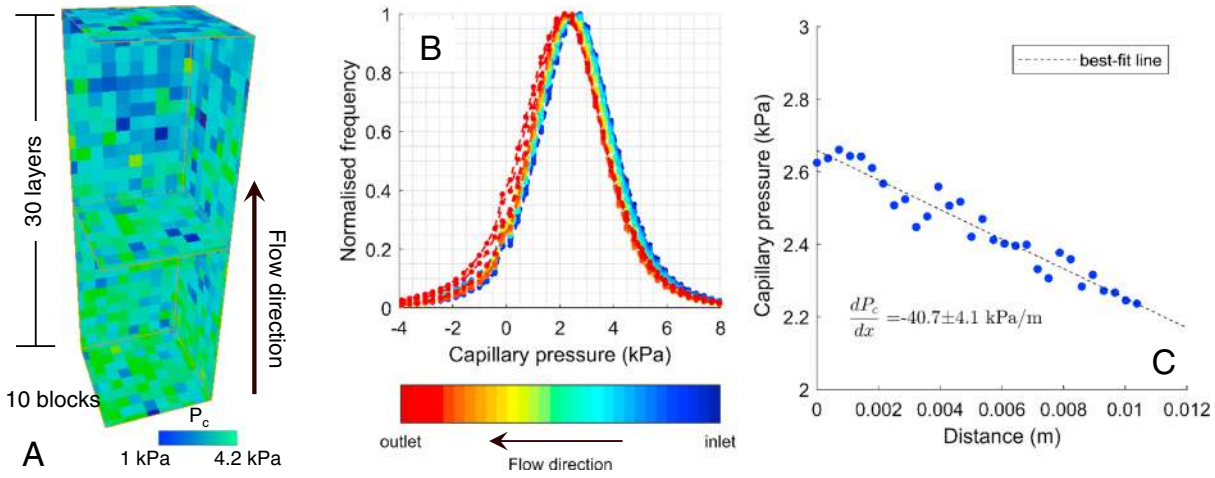

Figure 5. (a) Visualization of the average capillary pressure distribution for the entire volume (1,000 × 1,000 × 3,000 voxels, 3,000 subvolumes in total with a dimension of 100 × 100 × 100 voxels). Green indicates higher capillary pressure, while blue indicates lower capillary pressure. (b) The average capillary pressure distribution along the flow direction within the sample (30 blocks in length) showing a decrease in capillary pressure in the flow direction. The color map indicates the location where the average capillary pressure is calculated. (c) The average value of the capillary pressure along the sample with an estimated gradient of −40.7 ± 4.1 kPa/m. The error represents the 95% confidence bounds. Distance is measured along the direction of flow from the injection side of the imaged volume shown in Figure 1.

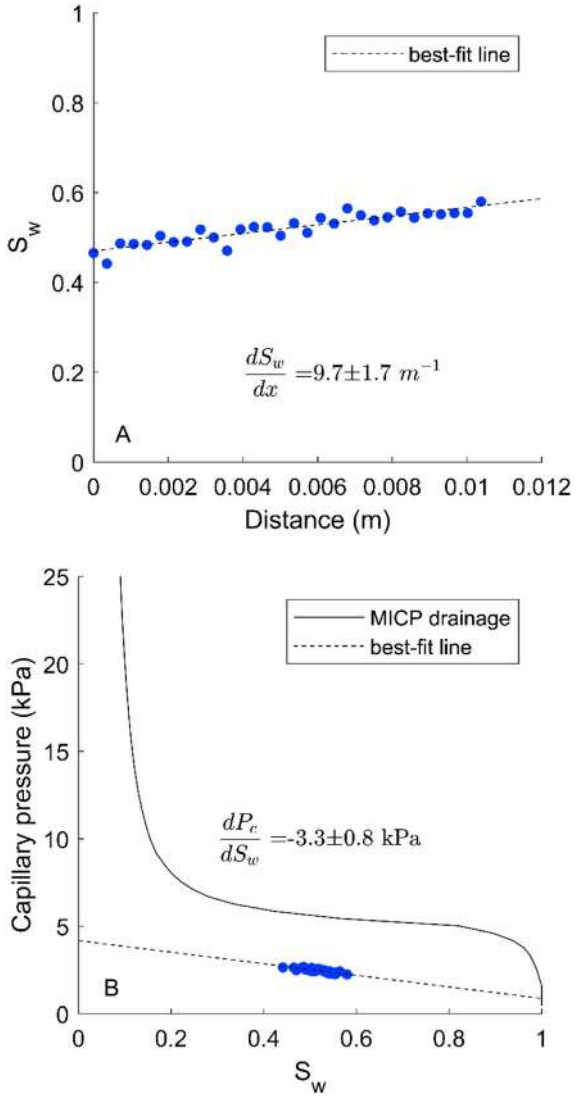

Figure 6. (a) Average saturation against distance (dS_w/dx) along the flow direction. (b) Capillary pressure changes against saturation (dP_c/dS_w) for each layer along the flow direction. The drainage capillary pressure from mercury injection is also shown. Both errors represent the 95% confidence bounds.

Table 1
Relative Permeability of the Oil and Brine Phases With and Without Capillary Pressure Calibration

f_w	S_w	R	k_{ro}	k_{rw} (uncorrected)	k_{rw} (corrected)
0	0.144	N/A	0.686	0	0
0.05	0.461	0.049	0.175	0.003	0.003
0.15	0.481	0.042	0.140	0.008	0.009
0.3	0.518	0.053	0.097	0.014	0.015
0.5	0.527	0.223	0.064	0.021	0.027
0.85	0.575	0.119	0.017	0.031	0.036
1	0.617	0.142	0	0.067	0.079

minimum radius is about 18 μm with a voxel size of 3.578 um (9.8 pixels). For a mean capillary pressure of 2.5 kPa obtained from curvature measurement, the uncertainty of the measurement for the mean capillary pressure is approximately ±0.2 kPa.

3.3. Quantification of Local Capillary Pressure Using Curvature Analysis

To obtain the local capillary pressure and its heterogeneity within the sample, the segmented volume (1,000 × 1,000 × 3,000 voxels; Figure 2b) was divided into 3,000 subvolumes (30 layers along the flow direction and 10 × 10 subvolumes per layer). Each subvolume has a dimension of 100 × 100 × 100 voxels. The smoothed oil/brine interface for the entire image (all 3000 subvolumes) was generated using a kernel size of 5 voxels for the smoothing process.

A visualization of the average capillary pressure distribution for all the subvolumes is shown in Figure 5. The capillary pressure for each subvolume was obtained from the mean of the curvature distribution using the Young-Laplace equation (9). The average capillary pressure across the core at each point in the direction of flow is also shown. Matching the trend in saturation, there is a trend of decreasing capillary pressure along the direction of flow. This suggests that a layer (1,000 × 1,000 × 100 voxels) is a suitable spatial scale over which to derive a capillary pressure-saturation relationship. The correction to estimates of relative permeability is obtained from equation (5) with R = 0.223. For the other fractional flows, the gradient in capillary pressure was smaller with, consequently, lower values of R.

We can also evaluate the consistency between the average curvature, capillary pressure, and saturation, shown in Figure 6, by evaluating the gradient of capillary pressure through:

$$\frac{dP_c}{dx} = \frac{dP_c}{dS_w}\frac{dS_w}{dx} \tag{10}$$

Substituting values (dP_c/dS_w = − 3.3 ± 0.8 kPa and dS_w/dx = 9.7 ± 1.7 m^{-1}) into equation (10), the estimated capillary pressure gradient along the sample is −32.3 ± 9.8 kPa/m, showing consistency in the relationship between capillary pressure measured by fluid curvature at the pore scale and the average fluid saturation averaged over the sample (−40.7 ± 4.1 kPa/m in Figure 5d). This suggests that using pore-scale curvature measurements can be used to assess capillary pressure and its variation throughout a sample. The values of R for each fraction flow were calculated and are shown in Table 1 in section 3.4.

The $P_c - S_w$ relationship evaluating data from all of the fractional flows is shown in Figure 7. The drainage capillary pressure was measured by mercury injection (MICP) and the value of interfacial tension has been scaled to the oil/brine system. We also plot drainage and imbibition capillary pressure measured using the porous plate technique on a Bentheimer sandstone by Raeesi et al. (2014) where we have again scaled the interfacial tension for comparison with the oil-brine fluid system used in this work. The drainage curves always lie above those for imbibition: contact angle hysteresis, trapping, and different pore-filling processes all contribute to lower capillary pressures for imbibition (Blunt, 2017).

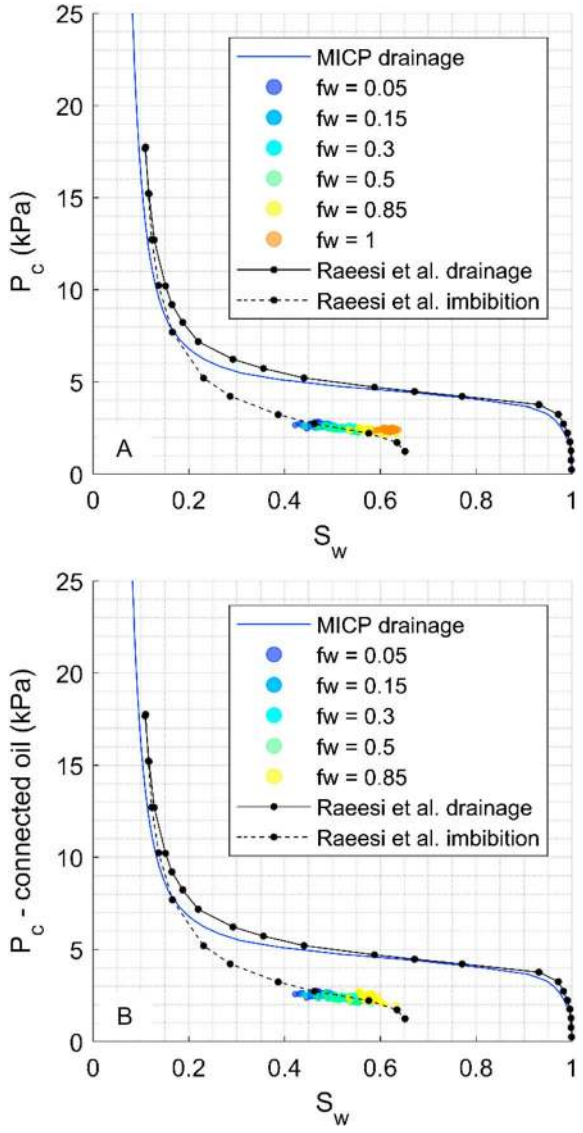

Figure 7. The average capillary pressure for (a) all of the oil phase and (b) the connected oil phase only against average saturation for each layer along the flow direction at different fractional flows. The capillary pressure for drainage from mercury injection (MICP) and the capillary pressure values for imbibition from curvature measurements are compared with measurements in a Bentheimer sandstone, for both drainage and imbibition, measured using a porous plate method by Raeesi et al. (2014). All the values have been corrected to the interfacial tension (51.5 mN/m) and contact angle (0°) for our system. For the air-mercury system, the interfacial tension was estimated to be 485 mN/m and the contact angle was estimated to be 140°. For the air-brine system used in Raeesi et al. (2014), the interfacial tension was 71 mN/m and the contact angle was assumed to be 0°. The initial brine saturation S_{wi} in this study was 0.144 and 0.103 in Raeesi et al. (2014).

We compare these results with our measured average capillary pressure across the whole volume and the variation of values within each layer (1,000 × 1,000 × 100 voxels). In this plot values for the full range of fractional flows are shown. It can be seen that in this water-wet system, during the imbibition process, there is a wide range of saturation within the sample; however, the capillary pressures at different fractional flows are similar and lower than the values for drainage. To observe a wider range of imbibition capillary pressure from curvature measurements, more fractional flow points need to be measured in the ranges $0 < f_w < 0.05$ and $0.85 < f_w < 1$.

Note that the porous plate and MICP measurements are in good agreement with the MICP data for drainage, while the porous plate and our curvature values for imbibition also correspond. This provides an independent check that our measurement of curvature can provide accurate estimates of continuum-scale capillary pressure.

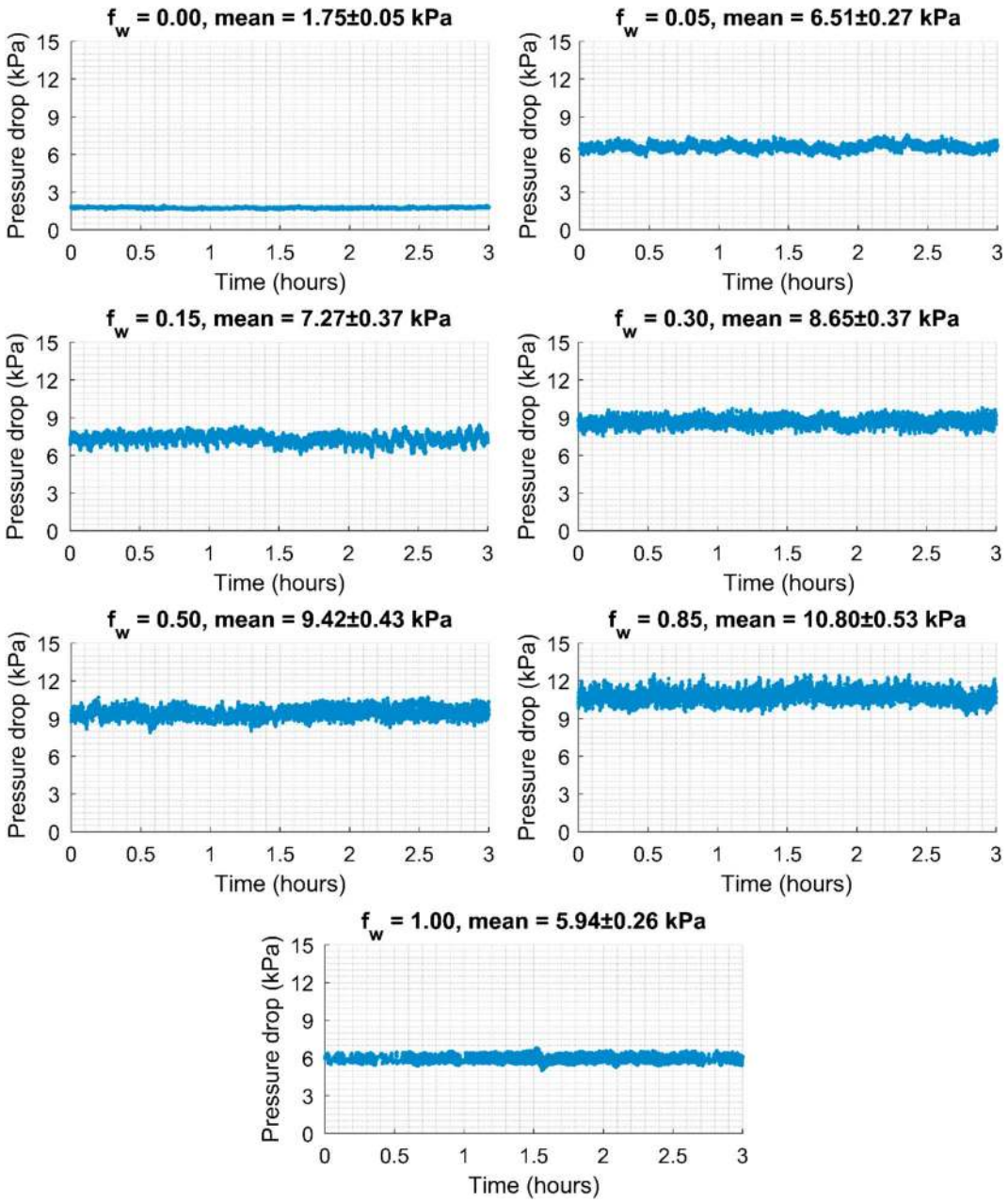

Figure 8. The measured pressure differential on the oil line using a differential pressure transducer at steady state for 3 hr before starting the scan at different fractional flows. The mean pressure drop and standard deviation are shown.

In Figure 7 we also show the capillary pressure when we consider only oil that is connected across the imaged volume. This excludes all the oil at $f_w = 1$, since the oil is at residual saturation, but has little effect on the results for the other fractional flows, where most of the oil is connected. This results in an even closer match to the data collected with the porous plate approach as it excludes some high values of capillary pressure in trapped ganglia, which are blobs of oil entirely surrounded by brine that cannot flow. The local curvature indicates the capillary pressure when the oil was trapped and not the prevailing value for the connected phases.

3.4. Estimate of Relative Permeability Corrected for the Capillary Pressure Gradient

Figure 8 shows the pressure differential across the entire rock sample at each fractional flow and the corresponding mean value and standard deviation during the final 3 hr of injection. In all cases, the constant pressure differential implies steady state while the core was scanned.

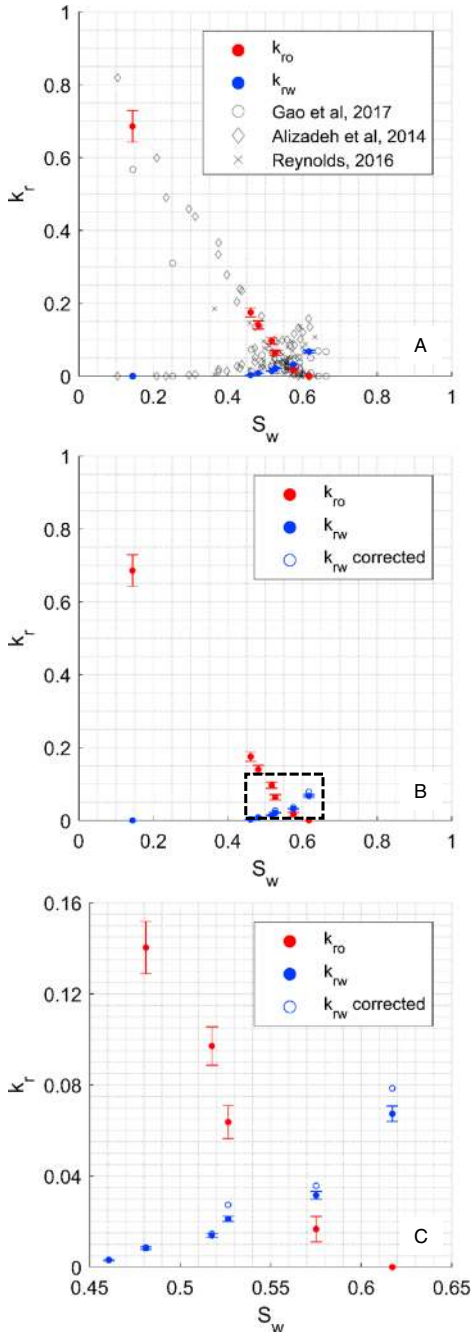

Figure 9. (a) Imbibition relative permeabilities calculated at steady state for brine-oil imbibition shown by the blue and red lines. The results are compared to the millimeter-scale experimental data by Gao et al. (2017), three sets of centimeter-scale experimental data by Alizadeh and Piri, (2014), and five sets of centimeter-scale experimental data by Reynolds, (2016). (b) Relative permeabilities for the oil and brine phase with and without the capillary pressure calibration. A zoom in plot for the highlighted region, shown in (c). The error bars consider uncertainties in the measurement of the length and diameter of the sample, the absolute permeability, pressure measurements, and the pump rates.

Using the same method as Gao et al. (2017), the relative permeability for both the oil and brine phases can be calculated, assuming that the capillary pressure is constant through the sample: this assumes that $R = 0$ in equation (8). Applying the method demonstrated in section 3.3, the capillary pressure differential along the sample at each fractional flow can be obtained. The correction to estimates of relative permeability are then obtained from equation (5) with $R = 0.223$. Using equations (7) and (8), and $\mu_o/\mu_w = 3$, the relative

permeability for each phase with and without the capillary pressure correction is shown in Table 1 and Figure 9. It can be seen that at high brine saturation, the capillary pressure effects have a larger impact on the relative permeability. The effects in this case are small because of the nature of the rock, which is homogeneous with a high permeability. In general, this allows for significant improvements in the accuracy of the determination of relative permeability with simultaneous but independent observations of relative permeability and capillary pressure.

Also note that the results are consistent with previous measurements of relative permeability, both on small samples of the same size as here (Gao et al., 2017) albeit without the capillary gradient correction, and steady state measurements on larger cores (Alizadeh & Piri, 2014; Reynolds, 2016). This again provides confidence in the results present here.

4. Conclusions and Outlook

We have demonstrated an experimental method to simultaneously measure capillary pressure and relative permeability during a steady state multiphase flow experiment through a homogeneous sandstone. The capillary pressures along the sample at different fractional flows have been obtained from the quantification of the fluid interface curvature. In this sample, while we see little variation in capillary pressure perpendicular to the flow direction, we do see a clear gradient in capillary pressure along the direction of flow. This is a manifestation of the well-known capillary end effect. While we can impose a constant fractional flow we cannot guarantee that the capillary pressure is locally constant. However, from our measurements we are able to quantify the effect and correct for it in the estimation of relative permeability. This is something that cannot be easily done using conventional methods unless an independent measurement of capillary pressure is made.

Overall, from a single experiment where macroscopic measurements are combined with pore-scale determinations of local curvature, we can specify both relative permeabilities and capillary pressure while accounting for capillary gradient effects. Our measurements agree with values in the literature measured on larger samples.

This method can be further applied in more heterogeneous cores by combining the direct measurement of the local capillary pressure using this curvature-based method with a numerical iterative approach to fully characterize and predict multiphase flow behavior in porous media (Jackson et al., 2018). This methodology can also be used to study more complex rocks and mixed-wet systems.

The main limitations for the study demonstrated in this work are twofold: limited sample size, and that only the pressure drop for the entire sample can be measured (the pressure drop in only the scanning region cannot be directly measured easily). However, with the continued development of laboratory-based micro-CT systems and synchrotron light sources, the trade-offs between image resolution and field of view can potentially be improved. This allows the design of new experimental approaches that would enable a larger sample size to be studied, while continuing to provide pore-scale information. Regarding the pressure measurement, the issue can be resolved by scanning the sample from inlet to outlet to capture the local capillary pressure for the entire sample. Furthermore, more fractional flow points are required to obtain a wider range of the capillary pressure and relative permeability.

Acknowledgments
We gratefully acknowledge funding from the Shell Digital Rocks program at Imperial College London. We thank Steffen Berg, Apostolos Georgiadis, and Ove Wilson from Shell for helpful and insightful comments on this work. The images acquired in this study can be downloaded from the Digital Rocks Portal: http://doi.org/10.17612/P7167R.

References

Akbarabadi, M., & Piri, M. (2013). Relative permeability hysteresis and capillary trapping characteristics of supercritical CO_2/brine systems: An experimental study at reservoir conditions. *Advances in Water Resources*, *52*, 190–206. https://doi.org/10.1016/j.advwatres.2012.06.014

Alhammadi, A. M., AlRatrout, A., Singh, K., Bijeljic, B., & Blunt, M. J. (2017). In situ characterization of mixed-wettability in a reservoir rock at subsurface conditions. *Scientific Reports*, *7*(1), 10753. https://doi.org/10.1038/s41598-017-10992-w

Alizadeh, A. H., & Piri, M. (2014). The effect of saturation history on three-phase relative permeability: An experimental study. *Water Resources Research*, *50*, 1636–1664. https://doi.org/10.1002/2013WR014914

Al-Khulaifi, Y., Lin, Q., Blunt, M. J., & Bijeljic, B. (2018). Reservoir-condition pore-scale imaging of dolomite reaction with supercritical CO_2 acidified brine: Effect of pore-structure on reaction rate using velocity distribution analysis. *International Journal of Greenhouse Gas Control*, *68*, 99–111. https://doi.org/10.1016/j.ijggc.2017.11.011

Al-Menhali, A. S., Menke, H. P., Blunt, M. J., & Krevor, S. C. (2016). Pore scale observations of trapped CO_2 in mixed-wet carbonate rock: Applications to storage in oil fields. *Environmental Science & Technology*, *50*(18), 10,282–10,290. https://doi.org/10.1021/acs.est.6b03111

AlRatrout, A., Raeini, A. Q., Bijeljic, B., & Blunt, M. J. (2017). Automatic measurement of contact angle in pore-space images. *Advances in Water Resources*, *109*, 158–169. https://doi.org/10.1016/j.advwatres.2017.07.018

Andreas, J. M., Hauser, E. A., & Tucker, W. B. (1937). Boundary tension by pendant drops 1. *The Journal of Physical Chemistry*, *42*(8), 1001–1019. https://doi.org/10.1021/j100903a002

Andrew, M., Bijeljic, B., & Blunt, M. J. (2014a). Pore-scale contact angle measurements at reservoir conditions using X-ray microtomography. *Advances in Water Resources*, *68*, 24–31. https://doi.org/10.1016/j.advwatres.2014.02.014

Andrew, M., Bijeljic, B., & Blunt, M. J. (2014b). Pore-by-pore capillary pressure measurements using X-ray microtomography at reservoir conditions: Curvature, snap-off, and remobilization of residual CO_2. *Water Resources Research*, *50*, 8760–8774. https://doi.org/10.1002/2014WR015970

Archer, J. S., & Wong, S. W. (1973). Use of a reservoir simulator to interpret laboratory waterflood data. *Society of Petroleum Engineers Journal*, *13*(06), 343–347. https://doi.org/10.2118/3551-PA

Armstrong, R. T., Pentland, C. H., Berg, S., Hummel, J., Lichau, D., & Bernard, L. (2012). Estimation of curvature from micro-CT liquid-liquid displacement studies with pore scale resolution. Int. Symp. Soc. Core anal. SCA2012-55, 6.

Armstrong, R. T., Porter, M. L., & Wildenschild, D. (2012). Linking pore-scale interfacial curvature to column-scale capillary pressure. *Advances in Water Resources*, *46*, 55–62. https://doi.org/10.1016/j.advwatres.2012.05.009

Arns, J.-Y., Arns, C. H., Sheppard, A. P., Sok, R. M., Knackstedt, M. A., & Val Pinczewski, W. (2003). Relative permeability from tomographic images: Effect of correlated heterogeneity. *Journal of Petroleum Science and Engineering*, *39*(3-4), 247–259. https://doi.org/10.1016/S0920-4105(03)00066-4

Berg, S., Ott, H., Klapp, S. A., Schwing, A., Neiteler, R., Brussee, N., et al. (2013). Real-time 3D imaging of Haines jumps in porous media flow. *Proceedings of the National Academy of Sciences*, *110*(10), 3755–3759. https://doi.org/10.1073/pnas.1221373110

Berg, S., Rücker, M., Ott, H., Georgiadis, A., van der Linde, H., Enzmann, F., et al. (2016). Connected pathway relative permeability from pore-scale imaging of imbibition. *Advances in Water Resources*, *90*, 24–35. https://doi.org/10.1016/j.advwatres.2016.01.010

Blunt, M. J. (2017). *Multiphase flow in permeable media: A pore-scale perspective*. Cambridge, United Kingdom: Cambridge University Press.

Blunt, M. J., Bijeljic, B., Dong, H., Gharbi, O., Iglauer, S., Mostaghimi, P., et al. (2013). Pore-scale imaging and modelling. *Advances in Water Resources*, *51*, 197–216. https://doi.org/10.1016/j.advwatres.2012.03.003

Buades, A., Coll, B., & Morel, J.-M. (2008). Nonlocal image and movie denoising. *International Journal of Computer Vision*, *76*(2), 123–139. https://doi.org/10.1007/s11263-007-0052-1

Burger, W., & Burge, M. J. (2010). *Principles of digital image processing: Core algorithms, undergraduate topics in computer science*. London: Springer.

Cnudde, V., & Boone, M. N. (2013). High-resolution X-ray computed tomography in geosciences: A review of the current technology and applications. *Earth-Science Reviews*, *123*, 1–17. https://doi.org/10.1016/j.earscirev.2013.04.003

Darling, T. (2005). *Well logging and formation evaluation*. Amsterdam, The Netherlands: Elsevier.

Fredd, C. N., & Fogler, H. S. (1998). Influence of transport and reaction on wormhole formation in porous media. *AICHE Journal*, *44*(9), 1933–1949. https://doi.org/10.1002/aic.690440902

Gao, Y., Lin, Q., Bijeljic, B., & Blunt, M. J. (2017). X-ray microtomography of intermittency in multiphase flow at steady state using a differential imaging method. *Water Resources Research*, *53*, 10,274–10,292. https://doi.org/10.1002/2017WR021736

Garing, C., de Chalendar, J. A., Voltolini, M., Ajo-Franklin, J. B., & Benson, S. M. (2017). Pore-scale capillary pressure analysis using multi-scale X-ray micromotography. *Advances in Water Resources*, *104*, 223–241. https://doi.org/10.1016/j.advwatres.2017.04.006

Gaus, I., Audigane, P., André, L., Lions, J., Jacquemet, N., Durst, P., et al. (2008). Geochemical and solute transport modelling for CO_2 storage, what to expect from it? *International Journal of Greenhouse Gas Control*, *2*(4), 605–625. https://doi.org/10.1016/j.ijggc.2008.02.011

Gelhar, L. W., Welty, C., & Rehfeldt, K. R. (1992). A critical review of data on field-scale dispersion in aquifers. *Water Resources Research*, *28*(7), 1955–1974. https://doi.org/10.1029/92WR00607

Hassler, G. L., & Brunner, E. (1945). Measurement of capillary pressures in small core samples. *Transactions of AIME*, *160*(01), 114–123. https://doi.org/10.2118/945114-G

Hege, H., Seebass, M., Stalling, D., & Zockler, M. (1997). A generalized marching cubes algorithm based on non-binary classifications. ZIB Prepr. sc-97-05.

Herring, A. L., Middleton, J., Walsh, R., Kingston, A., & Sheppard, A. (2017). Flow rate impacts on capillary pressure and interface curvature of connected and disconnected fluid phases during multiphase flow in sandstone. *Advances in Water Resources*, *107*, 460–469. https://doi.org/10.1016/j.advwatres.2017.05.011

Jackson, S. J., Agada, S., Reynolds, C. A., & Krevor, S. (2018). Characterizing drainage multiphase flow in heterogeneous sandstones. *Water Resources Research*, *54*, 3139–3161. https://doi.org/10.1029/2017WR022282

Jones, A. C., Arns, C. H., Sheppard, A. P., Hutmacher, D. W., Milthorpe, B. K., & Knackstedt, M. A. (2007). Assessment of bone ingrowth into porous biomaterials using micro-CT. *Biomaterials*, *28*(15), 2491–2504. https://doi.org/10.1016/j.biomaterials.2007.01.046

Kalam, M. Z., Al Hammadi, K., Wilson, O. B., Dernaika, M., & Samosir, H. (2006). Importance of porous plate measurements on carbonates at pseudo reservoir conditions, in: SCA2006-28, Presented at the 2006 SCA International Symposium, Trondheim, Norway.

Kennedy, M. (2015). *Practical petrophysics*. Netherlands: Elsevier.

Ketcham, R. A., & Carlson, W. D. (2001). Acquisition, optimization and interpretation of x-ray computed tomographic imagery: Applications to the geosciences. *Computational Geosciences*, *27*(4), 381–400. https://doi.org/10.1016/S0098-3004(00)00116-3

Krause, M. H. (2012). Modeling and investigation of the influence of capillary heterogeneity on multiphase flow of CO_2 and brine. (Doctoral dissertation, Stanford University).

Krevor, S. C. M., Pini, R., Zuo, L., & Benson, S. M. (2012). Relative permeability and trapping of CO_2 and water in sandstone rocks at reservoir conditions. *Water Resources Research*, *48*, W02532. https://doi.org/10.1029/2011WR010859

Lai, P., Moulton, K., & Krevor, S. (2015). Pore-scale heterogeneity in the mineral distribution and reactive surface area of porous rocks. *Chemical Geology*, *411*, 260–273. https://doi.org/10.1016/j.chemgeo.2015.07.010

Li, B., & Benson, S. M. (2015). Influence of small-scale heterogeneity on upward CO_2 plume migration in storage aquifers. *Advances in Water Resources*, *83*, 389–404. https://doi.org/10.1016/j.advwatres.2015.07.010

Li, T., Schlüter, S., Dragila, M. I., & Wildenschild, D. (2018). An improved method for estimating capillary pressure from 3D microtomography images and its application to the study of disconnected nonwetting phase. *Advances in Water Resources*, *114*, 249–260. https://doi.org/10.1016/j.advwatres.2018.02.012

Lin, Q., Al-Khulaifi, Y., Blunt, M. J., & Bijeljic, B. (2016). Quantification of sub-resolution porosity in carbonate rocks by applying high-salinity contrast brine using X-ray microtomography differential imaging. *Advances in Water Resources*, *96*, 306–322. https://doi.org/10.1016/j.advwatres.2016.08.002

Lin, Q., Andrew, M., Thompson, W., Blunt, M. J., & Bijeljic, B. (2018). Optimization of image quality and acquisition time for lab-based X-ray microtomography using an iterative reconstruction algorithm. *Advances in Water Resources*, *115*, 112–124. https://doi.org/10.1016/j.advwatres.2018.03.007

Lin, Q., Bijeljic, B., Rieke, H., & Blunt, M. J. (2017). Visualization and quantification of capillary drainage in the pore space of laminated sandstone by a porous plate method using differential imaging X-ray microtomography. *Water Resources Research*, *53*, 7457–7468. https://doi.org/10.1002/2017WR021083

Lin, Q., Neethling, S. J., Courtois, L., Dobson, K. J., & Lee, P. D. (2016). Multi-scale quantification of leaching performance using X-ray tomography. *Hydrometallurgy*, *164*, 265–277. https://doi.org/10.1016/j.hydromet.2016.06.020

Loeve, D., Wilschut, F., Hanea, R. H., Maas, J. G., van Hooff, P. M. E., van den Hoek, P. J., et al. (2011). Simultaneous determination of relative permeability and capillary pressure curves by assisted history matching several scale experiments. Int. Symp. Soc. Core Anal. (pp. 1–12).

Lorensen, W. E., & Cline, H. E. (1987). Marching cubes: A high resolution 3D surface construction algorithm. *ACM SIGGRAPH Computer Graphics*, *21*(4), 163–169. https://doi.org/10.1145/37402.37422

Lv, P., Liu, Y., Wang, Z., Liu, S., Jiang, L., Chen, J., & Song, Y. (2017). In situ local contact angle measurement in a CO_2–brine–sand system using microfocused X-ray CT. *Langmuir*, *33*(14), 3358–3366. https://doi.org/10.1021/acs.langmuir.6b04533

Masalmeh, S. K., & Jing, X. D. (2008). The importance of special core analysis in modelling remaining oil saturation in carbonate fields. In *Proceedings of the International Symposium of the Society of Core Analysis*.

Masalmeh, S. K., Jing, X. D., van Vark, W., Christiansen, S., Van der Weerd, H., & Van Dorp, J. (2004). Impact of SCAL (special core analysis) on carbonate reservoirs: How capillary forces can affect field performance predictions. *Petrophysics*, *45*, 403–413.

McPhee, C., Reed, J., & Zubizarreta, I. (2015). Best practice in coring and core analysis. In *Developments in Petroleum Science* (pp. 1–15). https://doi.org/10.1016/B978-0-444-63533-4.00001-9

Morrow, N., & Buckley, J. (2011). Improved oil recovery by low-salinity waterflooding. *Journal of Petroleum Technology*, *63*(05), 106–112. https://doi.org/10.2118/129421-JPT

Muskat, M., & Meres, M. W. (1936). The flow of heterogeneous fluids through porous media. *Physics (College. Park. Md).*, *7*(9), 346–363. https://doi.org/10.1063/1.1745403

Norouzi Apourvari, S., & Arns, C. H. (2016). Image-based relative permeability upscaling from the pore scale. *Advances in Water Resources*, *95*, 161–175. https://doi.org/10.1016/j.advwatres.2015.11.005

Parker, J. C. (1989). Multiphase flow and transport in porous media. *Reviews of Geophysics*, *27*(3), 311. https://doi.org/10.1029/RG027i003p00311

Pini, R., & Benson, S. M. (2013). Simultaneous determination of capillary pressure and relative permeability curves from core-flooding experiments with various fluid pairs. *Water Resources Research*, *49*, 3516–3530. https://doi.org/10.1002/wrcr.20274

Pini, R., Krevor, S. C. M., & Benson, S. M. (2012). Capillary pressure and heterogeneity for the CO2/water system in sandstone rocks at reservoir conditions. *Advances in Water Resources*, *38*, 48–59. https://doi.org/10.1016/j.advwatres.2011.12.007

Qajar, J., & Arns, C. H. (2016). Characterization of reactive flow-induced evolution of carbonate rocks using digital core analysis—Part 1: Assessment of pore-scale mineral dissolution and deposition. *Journal of Contaminant Hydrology*, *192*, 60–86. https://doi.org/10.1016/j.jconhyd.2016.06.005

Rabinovich, A., Itthisawatpan, K., & Durlofsky, L. J. (2015). Upscaling of CO_2 injection into brine with capillary heterogeneity effects. *Journal of Petroleum Science and Engineering*, *134*, 60–75. https://doi.org/10.1016/j.petrol.2015.07.021

Raeesi, B., Morrow, N. R., & Mason, G. (2014). Capillary pressure hysteresis behavior of three sandstones measured with a multistep outflow–inflow apparatus. *Vadose Zone Journal*, *13*(3). https://doi.org/10.2136/vzj2013.06.0097

Reyes, F., Lin, Q., Udoudo, O., Dodds, C., Lee, P. D., & Neethling, S. J. (2017). Calibrated X-ray micro-tomography for mineral ore quantification. *Minerals Engineering*, *110*, 122–130. https://doi.org/10.1016/j.mineng.2017.04.015

Reynolds, C. A. (2016). Two-phase flow behaviour and relative permeability between CO_2 and brine in sandstones at the pore and core scales. (Doctoral dissertation, Imperial College London).

Reynolds, C. A., Menke, H., Andrew, M., Blunt, M. J., & Krevor, S. (2017). Dynamic fluid connectivity during steady-state multiphase flow in a sandstone. *Proceedings of the National Academy of Sciences*, *114*(31), 8187–8192. https://doi.org/10.1073/pnas.1702834114

Richards, L. A. (1931). Capillary conduction of liquids through porous mediums. *Physics (College. Park. Md).*, *1*(5), 318–333. https://doi.org/10.1063/1.1745010

Saif, T., Lin, Q., Bijeljic, B., & Blunt, M. J. (2017). Microstructural imaging and characterization of oil shale before and after pyrolysis. *Fuel*, *197*, 562–574. https://doi.org/10.1016/j.fuel.2017.02.030

Schlüter, S., Berg, S., Rücker, M., Armstrong, R. T., Vogel, H.-J., Hilfer, R., & Wildenschild, D. (2016). Pore-scale displacement mechanisms as a source of hysteresis for two-phase flow in porous media. *Water Resources Research*, *52*, 2194–2205. https://doi.org/10.1002/2015WR018254

Sigmund, P. M., & McCaffery, F. G. (1979). An improved unsteady-state procedure for determining the relative-permeability characteristics of heterogeneous porous media (includes associated papers 8028 and 8777). *Society of Petroleum Engineers Journal*, *19*(01), 15–28. https://doi.org/10.2118/6720-PA

Stauffer, C. E. (1965). The measurement of surface tension by the pendant drop technique. *The Journal of Physical Chemistry*, *69*(6), 1933–1938. https://doi.org/10.1021/j100890a024

Whitaker, S. (1986). Flow in porous media I: A theoretical derivation of Darcy's law. *Transport in Porous Media*, *1*(1), 3–25. https://doi.org/10.1007/BF01036523

Zhou, D., Fayers, F. J., & Orr, F. M. (1997). Scaling of multiphase flow in simple heterogeneous porous media. *SPE Reservoir Engineering*, *12*(03), 173–178. https://doi.org/10.2118/27833-PA